



<http://www.diva-portal.org>

Postprint

This is the accepted version of a paper published in *Sensors and Actuators A-Physical*. This paper has been peer-reviewed but does not include the final publisher proof-corrections or journal pagination.

Citation for the original published paper (version of record):

Asiatici, M., Fischer, A C., Rodjegard, H., Haasl, S., Stemme, G. et al. (2016)
Capacitive inertial sensing at high temperatures of up to 400 degrees C
Sensors and Actuators A-Physical, 238: 361-368
<https://doi.org/10.1016/j.sna.2015.12.025>

Access to the published version may require subscription.

N.B. When citing this work, cite the original published paper.

Permanent link to this version:

<http://urn.kb.se/resolve?urn=urn:nbn:se:kth:diva-183657>

Capacitive Inertial Sensing at High Temperatures of up to 400 °C[☆]

Mikhail Asiatici^{a,b,*}, Andreas C. Fischer^{a,c}, Henrik Rödjegård^d, Sjoerd Haasl^a, Göran Stemme^a, Frank Niklaus^a

^a*KTH Royal Institute of Technology, School of Electrical Engineering, Department of Micro and Nanosystems, Stockholm, Sweden*

^b*EPFL Ecole Polytechnique Fédérale de Lausanne, School of Computer and Communication Sciences, Processor Architecture Laboratory, Lausanne, Switzerland*

^c*KIT Karlsruhe Institute of Technology, Institute of Nanotechnology, Karlsruhe, Germany*

^d*SenseAir AB, Stationsgatan 12, Delsbo, Sweden*

Abstract

High-temperature-resistant inertial sensors are increasingly requested in a variety of fields such as aerospace, automotive and energy. Capacitive detection is especially suitable for sensing at high temperatures due to its low intrinsic temperature dependence. In this paper, we present high-temperature measurements utilizing a capacitive accelerometer, thereby proving the feasibility of capacitive detection at temperatures of up to 400 °C. We describe the observed characteristics as the temperature is increased and propose an explanation of the physical mechanisms causing the temperature dependence of the sensor, which mainly involve the temperature dependence of the Young's modulus and of the viscosity and the pressure of the gas inside the sensor cavity. Therefore a static electromechanical model and a dynamic model that takes into account squeeze film damping were developed.

Keywords: high temperature, harsh environment, inertial sensors, capacitive detection, accelerometer

1. Introduction

Sensors working at high temperatures are of great interest in an increasing number of applications and markets [1]. In automotive applications, detection of temperature, pressure and vibrations close to the engine are essential

[☆]Published on Sensors and Actuators A: Physical 238, 361-368 (2015). <https://doi.org/10.1016/j.sna.2015.12.025>

*Corresponding author

Email addresses: mikhail.asiatici@ee.kth.se (Mikhail Asiatici), andreas.fischer@ee.kth.se (Andreas C. Fischer), henrik.rodjegard@senseair.se (Henrik Rödjegård), sjoerd.haasl@sth.kth.se (Sjoerd Haasl), goran.stemme@ee.kth.se (Göran Stemme), frank.niklaus@ee.kth.se (Frank Niklaus)

to improve its efficiency and reliability [1]. The wide operating temperature range of engines, $-40\text{ }^{\circ}\text{C}$ to $200\text{ }^{\circ}\text{C}$ [2], poses additional constraints in terms of temperature drifts and sensor reliability under thermal cycling compared to a continuous operation at a fixed high temperature. Measurement of tilt and vibrations in drilling tools at up to $200\text{ }^{\circ}\text{C}$ are important for the oil and gas industry [3, 4]. In aerospace technology, intelligent propulsion systems rely on continuous monitoring and adjustment of combustion conditions to decrease maintenance, increase safety and improve performance. This requires the use of electronics and sensors that are working above $300\text{ }^{\circ}\text{C}$ and up to $600\text{ }^{\circ}\text{C}$ [5]. Moreover, some environments encountered in space exploration are intrinsically harsh. For instance, the deployment of a lander on Venus has to be based on the availability of electronics and sensors suitable for long-term operation at $460\text{ }^{\circ}\text{C}$ [1].

Capacitive inertial sensors are especially attractive for high-temperature applications because of the inherently low temperature dependence of the capacitive sensing principle [1]. Indeed, capacitive inertial sensors rely on the change of electrical capacitance induced by a variation of the separation between two electrically biased plates or of their overlapping area when an external acceleration or angular rate is applied, and both quantities are only weakly dependent on temperature, mainly through thermal expansion of the solid sensor parts and of temperature-induced changes in the Young's modulus. This is an important advantage compared to e.g. piezoresistive transduction, in which the strong temperature dependence of the piezoresistive coefficients results in non-negligible temperature drifts of the output resistance that need to be compensated [6, 7] or eliminated by operating the piezoresistors at constant temperature, e.g. by utilizing micro-heaters [8]. Piezoelectric sensors are less sensitive to temperature and have been demonstrated for operation at up to $1250\text{ }^{\circ}\text{C}$ [9], but they show a band-pass response that limits their sensitivity at low frequencies [10].

Although capacitive detection appears to be in principle well suited for inertial sensing at high temperatures, several technological challenges need to be addressed in order to ensure that the sensor properly operates at extreme temperatures. First, all involved materials need to be mechanically and electrically stable along the desired operating temperature range. Secondly, if different materials are coupled, it is essential that their thermal expansion coefficients are reasonably well matched in order to not induce cracks, bending or unwanted displacements of the proof mass or of the cantilever spring as the temperature changes. These requirements can pose severe constraints on the choice of the materials and on the fabrication process, and such constraints are potentially part of the reasons why no capacitive inertial sensor for temperatures above $175\text{ }^{\circ}\text{C}$ has been demonstrated [11] and, as a consequence, no investigation of the phenomena that affect the behaviour of capacitive inertial sensors at high temperature has been performed.

Here, we present our measurements performed on a capacitive accelerometer at high temperatures of up to $400\text{ }^{\circ}\text{C}$. For our experiments we use the bare silicon MEMS sensor die from a commercial single-axis accelerometer module. While the packaged sensor module can operate only up to $125\text{ }^{\circ}\text{C}$, the bare

sensor die is mostly made of silicon and does not contain any active electronic device, thus it can withstand temperatures of above 400 °C. In this paper, we first describe the sensor structure, with special emphasis on the design elements that are most likely to have a strong impact on the temperature dependence. Secondly, an electromechanical model is developed to gain insight in the sensor response and possible causes for temperature drifts. Static and dynamic measurements of the sensor at different temperatures are presented and a physical interpretation is provided. Our findings prove the feasibility of capacitive detection for temperatures of up to at least 400 °C and they will be useful to improve the quality and the reliability of future designs for capacitive inertial sensors that can operate at high temperatures.

2. Accelerometer structure and model

Sensors composed of a small set of materials, all of which stable at high temperature, are expected to provide the best performances under wide temperature ranges as stresses and bending due to mismatches of thermal expansion between materials are limited. As for the main structural material, silicon represents a promising candidate as it is mechanically stable at temperatures of up to at least 500 °C [12]. Therefore, we have performed our measurements on a capacitive accelerometer (Colibrys MS9002.D MEMS sensor) whose structural design and materials are depicted in Figure 1.

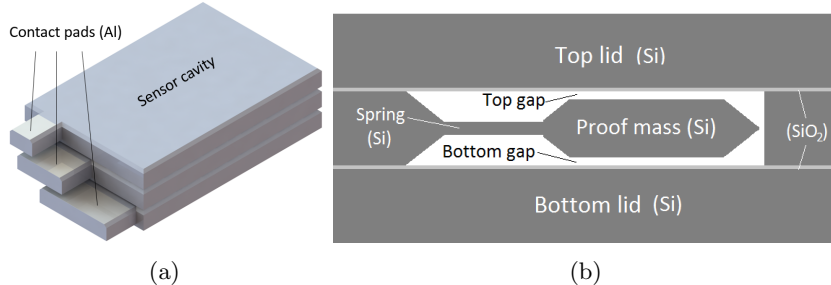


Figure 1: (a) 3D model of the accelerometer and (b): Schematic of the accelerometer cross section.

The accelerometer is composed of a stack of three fusion-bonded silicon layers. The central wafer is structured on both sides by silicon etching to release the mass and to obtain the spring, which consists of a thin silicon cantilever clamped at one edge. An SEM image of the top view of the spring-mass system of the accelerometer is shown in Figure 2. The top and bottom wafers enclose the spring and the mass in a sealed cavity and constitute the fixed electrodes of the differential capacitors. The cavity contains a low-pressure atmosphere that allows controlled viscous squeeze film damping. With this configuration, the mass is moving vertically when an out of plane acceleration is applied, and this results in a change of the widths of the top and bottom gaps and thereby of the related capacitances.

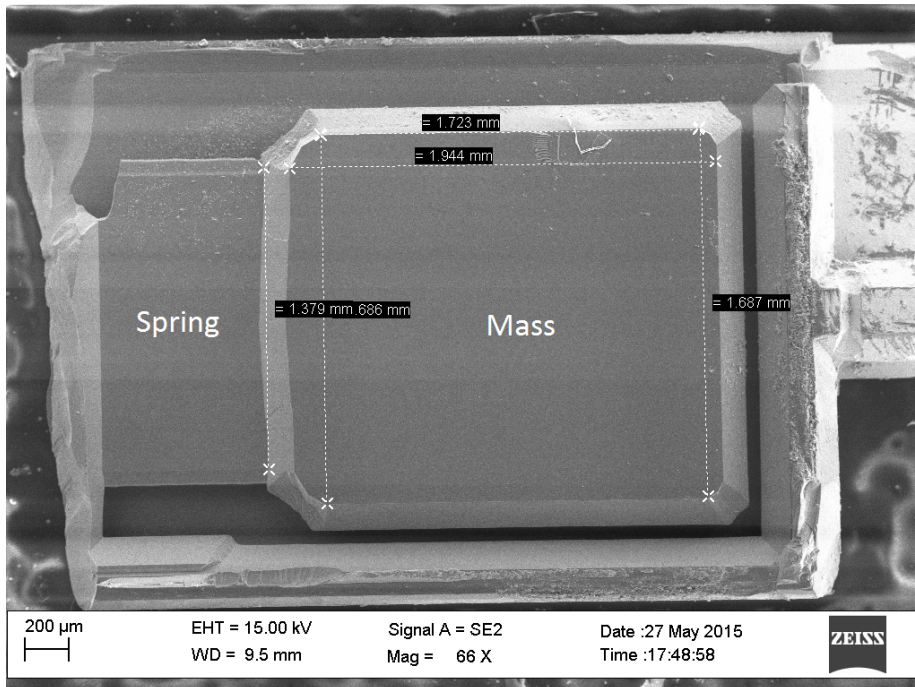


Figure 2: SEM image of the top view of the spring-mass system, after removal of the top wafer.

The sensor is made of silicon except for an approximately $1\ \mu\text{m}$ thick layer of SiO_2 on the surfaces of the top and bottom wafers facing the central wafer, as revealed by Energy Dispersive Spectroscopy (EDS) analysis. This structure ensures electrical insulations between the wafers and avoids short circuits between the proof mass and the fixed electrodes in case of pull in [13]. In addition, a carbon-based thin layer is present on all the surfaces inside the cavity, functioning as an anti stiction layer [14]. All the electrical connections between the movable and static electrodes and the respective aluminium pads are provided by the silicon substrates. No diffusion is expected to occur from the metallizations up to at least $500\ ^\circ\text{C}$ [15].

Figure 3 depicts the capacitive model of the sensor as seen from the external terminals. Subscripts t and b denote top and bottom capacitances respectively. Each of these is in turn decomposed in a parallel and a gap capacitance, denoted by subscripts p and g , respectively. The parallel capacitances are associated to the interfaces between the bonded substrates with the intermediate SiO_2 layer and to the parasitic capacitances between the pads. The gap capacitances are the only capacitive components that depend on the acceleration, with the dependencies resulting from the changing air gaps between the mass and each of the fixed electrodes (top and bottom).

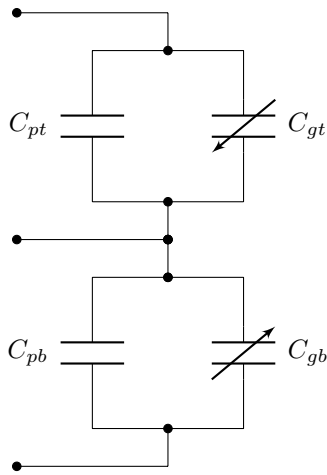


Figure 3: Proposed model for the accelerometer capacitances as seen from the external terminals.

To describe the effects of varying temperature on the system response, an electromechanical model of the accelerometer has been developed. The model was also used to provide an interpretation of the measurement results obtained by moving the proof mass with an electrostatic force. Since the proof mass constitutes most of the system mass, applying a force $F = ma$ on the proof mass only, m being the mass of the proof mass, produces essentially the same results as applying an acceleration a to the entire system. The model equations that have been derived are thus expressed in terms of F instead of a as this makes

the model applicable also when the mass will be displaced by an electrostatic force.

To qualitatively describe the motion of the spring-mass system and to select the relevant quantities to be included in the semi-analytic model, a 3D Finite Element (FE) model in COMSOL Multiphysics 5.1 has been used. Figure 4 shows the geometry that has been simulated and Table 1 depicts the geometrical parameters that have been used for the model. By taking advantage of the symmetry of the device, only half of the spring-mass system was simulated. Silicon has been modelled as an isotropic material with a Young’s modulus $E = E_{110} = 169$ GPa and a Poisson’s ratio of $\nu = 0.0642$ [16]. This approximation has been chosen instead of a fully anisotropic model because it reduces the number of parameters to be considered in the subsequent semi-analytic model while providing results that deviate by less than 3% under typical loads for this device according to our FE simulations.

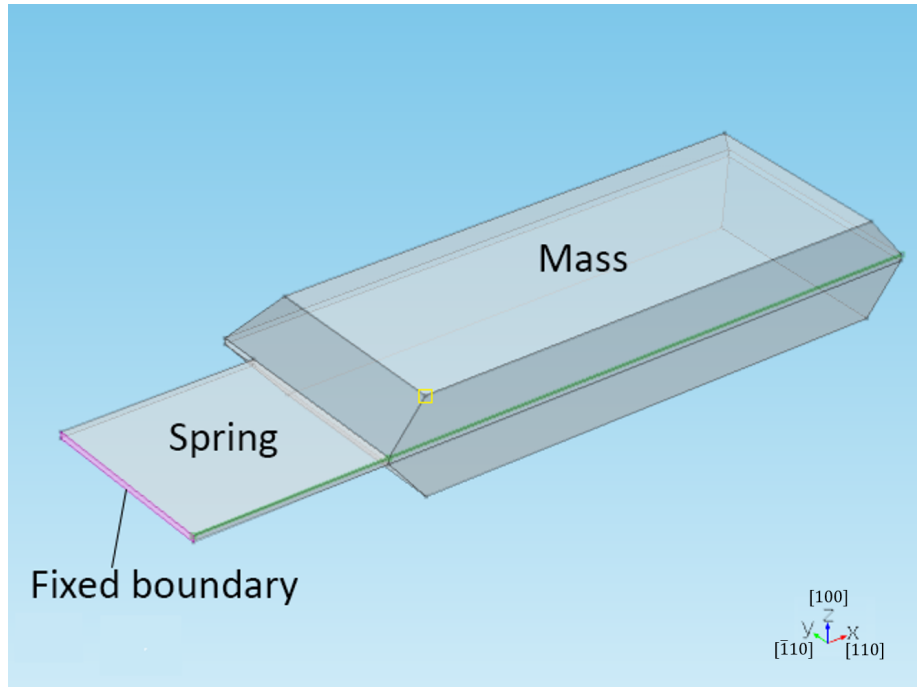


Figure 4: 3D geometry and reference system used for the modelling of the accelerometer.

For accelerations of up to 1 g, all the bending is concentrated in the spring, while the mass undergoes only a rigid translation along z and rotation around y . Because of the mass rotation, the gaps change linearly along the mass length. Although the tilt angle of the mass is very small, approximately 10^{-4} rad for a 1 g acceleration, an l_x that is three orders of magnitude larger than the expected gaps results in a non-negligible gap difference at the two ends of the proof mass. Therefore, both the mass vertical displacement at the bottom-left corner of the

Mass length l_x	1.83 mm
Mass width l_y	1.53 mm
Mass thickness l_z	375 μm
Spring length $l_{b,x}$	0.735 mm
Spring width $l_{b,y}$	1.49 mm
Spring thickness $l_{b,z}$	24 μm
Slanted sidewalls angle α	51°

Table 1: Geometrical parameters of the spring-mass system simulated in COMSOL. Mass length and mass width refer to the top and bottom boundaries.

movable plate as highlighted in yellow in Figure 4, Δz , and the tilt angle β , identified by $p = \tan(\beta)$, are needed to describe the motion of the proof mass. With the notations shown in Figure 5, the gap changes linearly along the x axis from $g_0 - \Delta z$ to $g_0 - \Delta z - pl_x$, where g_0 represents the nominal gap, i.e. the uniform gap width when no force is applied to the proof mass.

According to the FE model, at steady state and for accelerations of up to 1 g, Δz and p can be expressed as:

$$\Delta z = c_z F \quad (1a)$$

$$p = c_p F \quad (1b)$$

with $c_z = 1.92 \times 10^{-3} \text{ m/N}$ and $c_p = 3.57 \text{ N}^{-1}$.

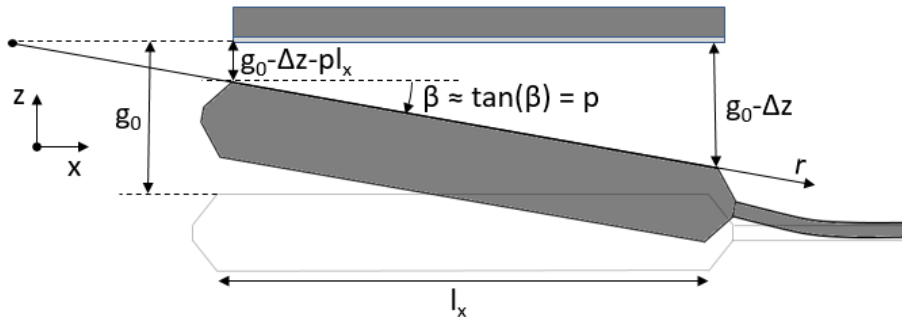


Figure 5: Reference frame used to derive the capacitance and the electrostatic force in the sensor.

The presence of the SiO_2 layer and the non-negligible mass tilting result in an electric field, and thus a capacitance and an electrostatic force, which deviate significantly from the common assumption of a parallel plate capacitor with a single dielectric. Tay et al. derived the expressions for the capacitance and the electrostatic force in a tilted plate capacitor with a single dielectric [17]. With the notations given in Figure 5, the capacitance and the electrostatic force can be expressed as:

$$C_g = \epsilon_0 \frac{l_y}{p} \ln \left(\frac{g_0 - \Delta z}{g_0 - \Delta z - pl_x} \right) \quad (2a)$$

$$F_{el} = \epsilon_0 \frac{l_x l_y V^2}{2(g_0 - \Delta z)(g_0 - \Delta z - pl_x)} \quad (2b)$$

For this sensor, which contains a SiO_2 layer (thickness $t_{ox} = 1 \mu\text{m}$, dielectric constant $\epsilon_{ox} = 3.9\epsilon_0$) in series with the air gap, the charge per unit area on either the movable or the fixed electrode can be computed as $\sigma(r) = \epsilon E(r)$, where the electric field $E(r)$ can be derived by taking into account the continuity of the perpendicular component of the electric displacement D at the interface between air and SiO_2 . This results in:

$$\sigma(r) = \epsilon_0 \epsilon_{ox} \frac{V}{\epsilon_0 t_{ox} + \epsilon_{ox} \beta r} \quad (3)$$

By applying the same procedure described by Tay et al., with $\sigma(r)$ given by Equation 3 and for small β , the capacitance and the electrostatic force with an SiO_2 layer can be expressed as:

$$C_g = \epsilon_0 \frac{l_y}{p} \ln \left(\frac{\epsilon_{ox}(g_0 - \Delta z) + \epsilon_0 t_{ox}}{\epsilon_{ox}(g_0 - \Delta z - pl_x) + \epsilon_0 t_{ox}} \right) \quad (4a)$$

$$F_{el} = \frac{\epsilon_0 \epsilon_{ox}^2 l_x l_y V^2}{2(\epsilon_{ox}(g_0 - \Delta z) + \epsilon_0 t_{ox})(\epsilon_{ox}(g_0 - \Delta z - pl_x) + \epsilon_0 t_{ox})} \quad (4b)$$

It is worth noting that Equations 4a and 4b can be obtained from Equations 2a and 2b by replacing g_0 with $g_{eq} = g_0 + \frac{\epsilon_0}{\epsilon_{ox}} t_{ox}$. This involves that g_0 and t_{ox} cannot be obtained independently only by fitting the electrical measurements.

For $\Delta z \ll g_0$ and $\Delta z + pl_x \ll g_0$, Equation 4a can be further simplified as:

$$C_g \approx \epsilon_0 \frac{l_x l_y}{g_{eq} - \Delta z - \frac{pl_x}{2}} = \epsilon_0 \frac{l_x l_y}{g_{eq} - \left(c_z + \frac{c_p l_x}{2} \right) F} \quad (5)$$

which is equivalent to a parallel plate capacitance whose gap corresponds to the gap in the middle of the proof mass along x and where the transduction of F to C_g can be essentially accounted for by a single compliance $c = c_z + \frac{c_p l_x}{2} = 5.19 \times 10^{-3} \text{ m/N}$.

Tilting of the mass p and vertical displacement of the mass Δz resulting from a static voltage V can be obtained by solving Equations 1a, 1b and 4b iteratively. Additional forces, due for instance to gravity, can be easily taken into account in the F term in Equation 1a and 1b. Once convergence is reached, the resulting C_g can be calculated according to Equation 4a.

The dynamic behaviour of the accelerometer will be strongly influenced by the fluid in the sensor cavity as it reacts to the mass motion. This effect, known as squeeze film damping, is described by the Reynolds equation, a non-linear partial differential equation [18]. Blech et al. linearized and solved this equation under the assumption that the mass displacement is parallel to the fixed electrode and small compared to the average gap, and that the pressure change

induced by the motion is small compared to the static pressure. Under these assumptions, the force can be decomposed in a viscous and a damping term, in phase with mass velocity and displacement respectively, which depend on frequency, geometry (gap and plate area) and gas properties (pressure and viscosity) [19]. These forces have been taken into account in an electrical equivalent model for a capacitive accelerometer by Veijola et al. [20], which will be used here to provide an interpretation of the frequency response of the accelerometer, assuming that mass tilt can be neglected from the point of view of fluid dynamics inside the cavity.

3. Measurement results and discussion

The accelerometer die has been characterized on a probe station containing a high-temperature chuck (Signatone S-1060R). The characterization was done at room temperature and between temperatures of 100 °C and 400 °C with 50 °C steps. For each temperature, two C(V) curves (for the top and bottom capacitances) and a frequency response have been collected. No significant thermal hysteresis has been observed from these measurements.

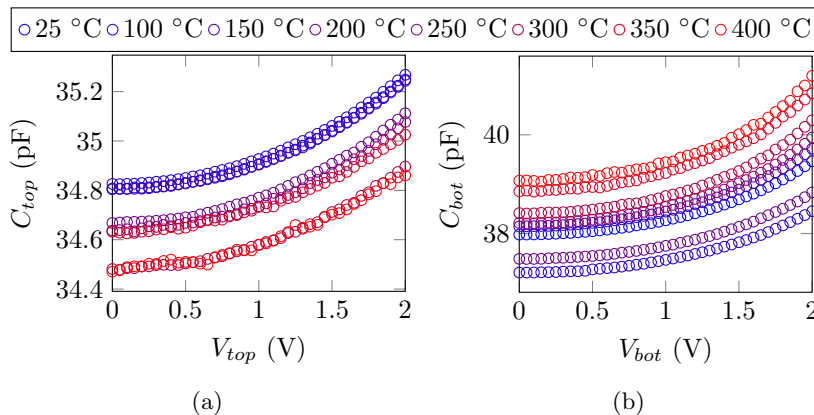


Figure 6: C(V) curves measured on (a) top and (b) bottom capacitances of the accelerometer.

For the C(V) measurements, an LCR meter (HP 4284A, Cs-Rs model, long integration time, 1 MHz signal with 100 mV RMS amplitude) was used to measure top and bottom capacitances. Before every measurement, an open compensation has been performed with the probes raised above the pads. The LCR meter was controlled by a LabVIEW interface that logged the measured capacitances while the DC bias was swept from 0 V to 2 V and back again to 0 V with 50 mV steps. Since no hysteresis has been found in this voltage range, the forward and backward curves have been averaged.

As it can be seen in the measured C(V) curves in Figure 6a and 6b, the top capacitance decreases with temperature, whereas the bottom capacitance increases. Based on the model developed, temperature could affect the sensor

through a change in all the physical dimensions because of thermal expansion. The average linear coefficient of thermal expansion of silicon between 25 °C and 400 °C is 3.42 ppm/°C [21, Equation 5], resulting in a relative expansion of 0.13%. Since all the capacitances and the electrostatic force are proportional to a length (c.f. Equation 4a and 4b respectively), an increase in all the capacitances and a progressive bending of the C(V) curves are expected as the temperature increases. The relative expansion of 0.13% is however not enough to explain the decrease in the top capacitance, while the bottom capacitance follows the opposite trend with temperature, increasing instead of decreasing.

A second effect could occur through changes in the transduction constants c_z and c_p and therefore in the compliance $c = c_z + \frac{c_p l_x}{2}$. Indeed, the FE model revealed that both thermal expansion and changes in the [110] Young's modulus can affect c . In particular, the finite element model showed that a 1% increase of all the geometrical dimensions or of the [110] Young's modulus results in a -1.18% and -0.99% change of c , respectively. Between the two effects, the latter is expected to be dominating as the Young's modulus of silicon along the [110] direction decreases by 6% from 25 °C to 400 °C [22, Section 5]. This results in a 6% increase of c , which is more than one order of magnitude larger than the effect on c due to thermal expansion of silicon. A more compliant spring will result in an increased mass displacement under the influence of the gravity of Earth, which can explain the increase of the bottom capacitance and the decrease of the top capacitance as the temperature increases. Secondly, electrostatic forces caused by the same voltage would cause larger displacements, resulting in an increased change of capacitance along the C(V) curves as the voltage is increased. In the measurements, this trend is especially evident for the bottom capacitance.

To obtain quantitative information from the measurements and to test the hypothesis of temperature-induced spring softening, the curves have been fitted with the equations developed in Section 2. In particular, the nominal gap width g_0 and the parallel capacitance C_p have been constrained to be identical for all the measurements corresponding to the same capacitance (top or bottom), as they are physically not expected to change with temperature. On the other hand, the compliance has been allowed to change for every curve to account for the possible changes due to temperature. This has been implemented by introducing a constant c_T that multiplies both c_z and c_p as a fit parameter. To take into account Earth's gravity when fitting the top and bottom capacitance C(V) curves, an additional force term $F_g = mg$ has been respectively subtracted from or added to the total force F before computing the mass displacement and tilt (Equations 1a and 1b).

The results of the fit are summarized in Table 2 and Figure 7. The overall trend for the compliance coefficient c_T is to increase with temperature in both the top and the bottom capacitance. The outliers have been attributed to measurement errors under the form of parasitic parallel capacitances not correctly compensated by the open compensation of the LCR meter. Indeed, physical changes in the sensors at specific temperatures would cause the outliers to appear in both curves at the same temperature, whereas the measured outliers

appear at different temperatures in the top and bottom capacitance measurements. Moreover, the fitting with the static model appeared to be sensitive to additive capacitive noise when the procedure has been tested on $C(V)$ curves generated from COMSOL.

The overall increasing trend for c_T is compatible with the expected thermal expansion and reduction in Young's modulus with increasing temperature. To verify if the temperature-induced drifts in c_T can be quantitatively explained by these two phenomena, they have subsequently been explicitly included in the model during the fitting. Thermal expansion has been taken into account on all the lengths in the model by using a temperature-dependent coefficient of thermal expansion for silicon [21, Equation 5]. As expected, the effect of thermal expansion alone is almost negligible. The temperature dependence of the Young's modulus has been taken into account by replacing c_T with $c_T' \frac{E_{110}(25^\circ C)}{E_{110}(T)}$, with $E_{110}(T)$ from literature [22, Section 5]. The temperature-induced increase of c_T' is smaller than the increase of c_T , although the trend could be only partially compensated by accounting for the thermal expansion and the decrease of Young's modulus.

	Top	Bottom
C_p	(23.0 ± 0.2) pF	(23 ± 1) pF
g_0	(1.69 ± 0.03) μm	(1.6 ± 0.2) μm

Table 2: C_p and g_0 from the fit of the $C(V)$ curves when thermal expansion and reduction of Young's modulus with increasing temperature are taken into account. The uncertainties correspond to the standard deviation obtained from the estimation of the covariance matrix based on the Jacobian at the optimum point.

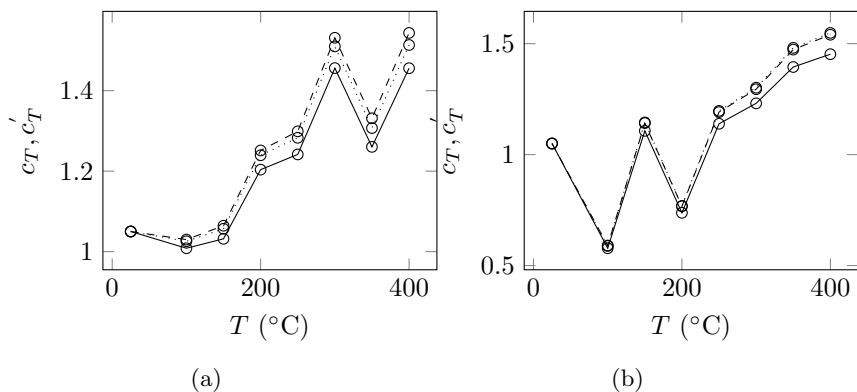


Figure 7: c_T and c_T' from the fit of the measured $C(V)$ curves of the (a) top and (b) bottom capacitors. Dotted lines: no compensation for thermal effects. Dashed lines: thermal expansion included. Solid lines: thermal expansion and Young's modulus decrease included.

A possible additional contribution to the increase of compliance could be a change in the properties of the carbon-based antistiction layer on the surface

of the spring. A strong temperature-induced reduction of Young's modulus for such layers or even a thermal degradation could significantly affect the overall spring compliance. This would suggest that the choice of the materials inside the sensor plays a crucial role in determining the temperature sensitivity of the sensor response.

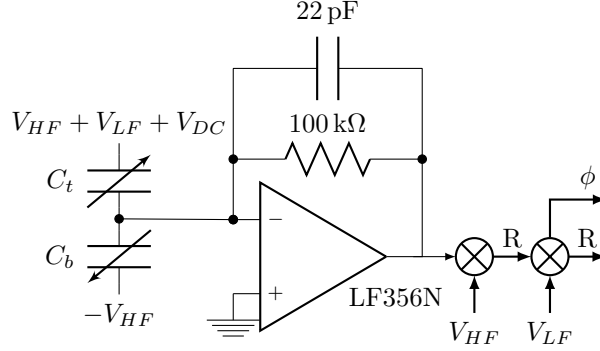


Figure 8: Set-up used for the dynamic characterization of the accelerometer. The two demodulators at the end of the signal chain include each a mixer and a low pass filter.

To determine whether temperature has an impact also on the dynamic response of the sensor, a lock-in amplifier (Zurich Instruments HF2LI) connected as shown in Figure 8 has been used to perform a frequency response measurement. V_{HF} and V_{LF} are sinusoidal voltages with 100 mV peak amplitude; V_{HF} is a 100 kHz signal used to read out the capacitance variations and V_{LF} is swept from 10 Hz to 2.5 kHz to actuate the mass. Since the charge amplifier biases the proof mass at virtual ground, the electrostatic force acting on the mass, positive towards the top electrode, can be calculated as:

$$F \propto \frac{1}{2}(V_{LFp}^2) + V_{DC}^2 + V_{LFp}V_{DC}\sin(\omega_{LF}t) - \frac{1}{2}V_{LFp}^2\cos(2\omega_{LF}t) + F_{HF} \quad (6)$$

where subscripts p denote peak voltages. F_{HF} includes all the terms at frequencies higher than $2\omega_{LF}$ that are filtered out by the sensor as they are well above the resonance frequency, 1.4 kHz [23]. V_{DC} has been set to 2 V: in this way, the force term at $2\omega_{LF}$ can be neglected and the dynamic force term can be approximated with the term at ω_{LF} alone. V_{LFp} and V_{HFp} have been made as small as possible in order to minimize signal distortions due to the feedback effect of the mass displacement on the electrostatic force (Equation 4b) and to ensure that the measured capacitance variations reflect the variations in mass displacement with good linearity.

Equation 7 describes the voltage at the output of the charge amplifier. A first demodulation with V_{HF} extracts the voltage component proportional to

$C_t - C_b$, which is in turn compared to V_{LF} by the second demodulator in terms of amplitude ratio $A = R/V_{LF}$ and phase shift ϕ .

$$V_{out} = -\frac{1}{C_f} (V_H \sin(\omega_H t) (C_t - C_b) + V_L \sin(\omega_L t) C_t) \quad (7)$$

Figure 9a and 9b show the frequency response of the sensor for temperatures of up to 400 °C. Each curve has been fitted with the response of a 3rd order linear system: at all the temperatures, the identified systems have a real pole and a complex conjugate pole pair, associated to squeeze film damping and mechanical resonance of the spring-mass system respectively. The pole due to RC filtering is expected to be in the order of tens of megahertz as the series resistance between the pads and the capacitors is in the order of a few hundreds of ohm according to the static LCR measurements.

As the temperature increases, both the frequency of the real pole and the quality factor of the complex conjugate pole pair decrease. A direct fit of the curves with the Veijola model has been attempted by using m as mass, $(c_T c \frac{E_{110}(25^\circ C)}{E_{110}(T)})^{-1}$ as spring constant and the gaps g_0 from the fit of the C(V) curves. For the model we have assumed that the cavity is filled with dry air, with the mean free path and the viscosity expressed by Equations 8a [24] and 8b [25, 20] respectively:

$$\lambda = \lambda_0 \frac{P_0}{P_{ref}} \quad (8a)$$

$$\eta = \frac{\eta_0}{1 + 9.638(\lambda/g_0)^{1.159}} \left(\frac{T}{T_{ref}} \right)^{1.5} \frac{T_{ref} + S}{T + S} \quad (8b)$$

with $\lambda_0 = 69.1$ nm, $\eta_0 = 18.6$ μ Pa s [26], $P_{ref} = 10^5$ Pa, $T_{ref} = 298.15$ K, $S = 110.4$ K [25] and T expressed in kelvin. The pressure at room temperature P_0 has been set as a fit parameter, while the pressure $P(T)$ involved in the Veijola model has been calculated as $P = P_0 T / T_{ref}$ from the ideal gas law. As the gas volume is constant, λ does not depend on temperature but only on the initial pressure P_0 (λ only depends on the number density of the gas [24] which is set when the cavity is sealed). On the other hand, an increase of temperature will result in an increase of both pressure and viscosity. However, the fit did not provide results that are coherent with the sensor geometry and the C(V) measurements. This could be due to a non-negligible impact of the mass tilting, which would violate one of the main assumptions on which the Veijola model is based. Moreover, the anti stiction layers are also likely to affect the dynamic response of the sensor. It is however worth noting that, for the air parameters above and assuming a pressure of 1 mbar, the frequency response of the corresponding Veijola model up to at least 10 kHz is dominated by a real and a complex conjugate pole pair as for the linear systems identified from the frequency measurements. Moreover, as shown in Figure 9c and 9d, the trends with temperature are comparable to the ones observed in the sensor, especially when both the change in c and the effects of temperature on the gas properties are considered. This suggests that a very low gas pressure inside the sensor

cavity can be a way to reduce the influence of temperature on the dynamic response of the sensor by making pressure and viscosity negligible, regardless of the temperature.

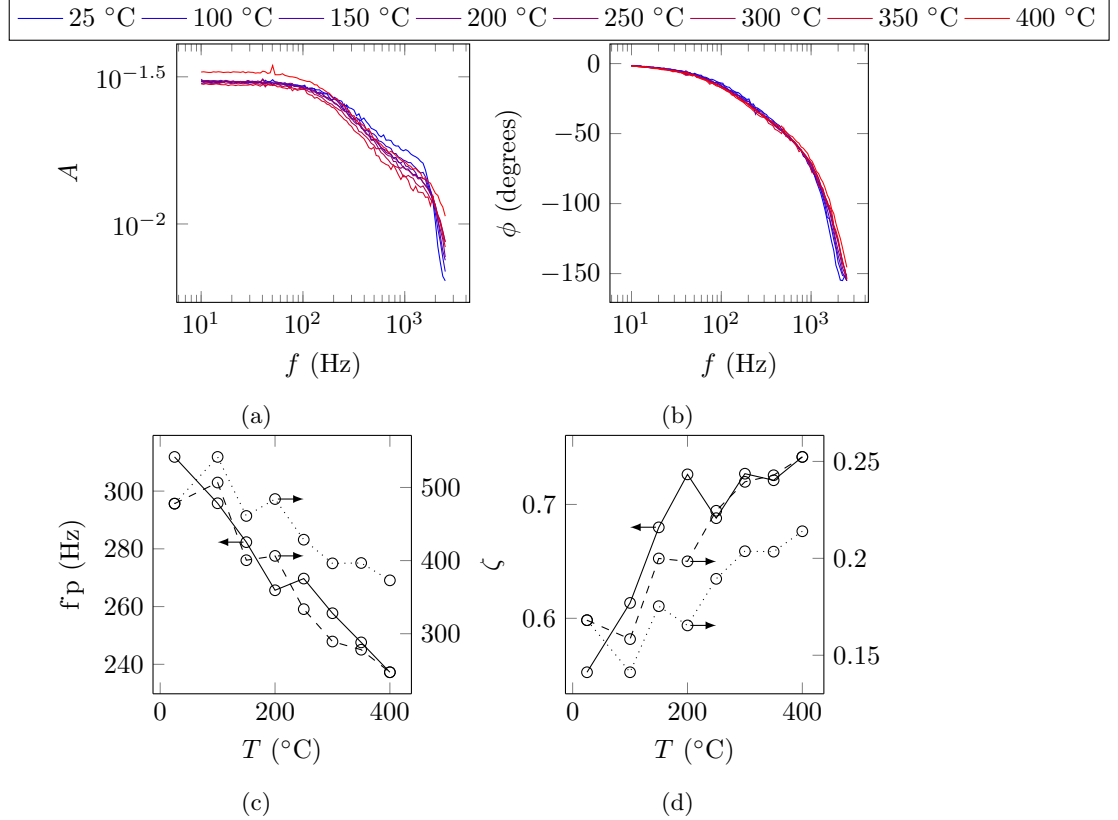


Figure 9: (a, b) Measured frequency response. (c, d): Real pole and dissipation factor ($\zeta = 1/(2Q)$) from a fit of the measured frequency response with a 3rd order linear system (solid) and from the Veijola model with c_T from Figure 7 (average between top and bottom capacitance c_T) with constant (dotted) and temperature dependent (dashed) gas pressure and viscosity.

4. Conclusion

A static model for a tilted plate capacitor with an oxide layer has been developed and high temperature measurements of a capacitive accelerometer proved the feasibility of reliable capacitive transduction at up to 400 °C. As the temperature increases, the static capacitances show trends that are in agreement with an increase of the spring compliance due to a decrease in the Young's modulus of silicon. Our model suggests that additional phenomena are also affecting the

spring compliance of the sensor used, which could be due to drifts from degradation of the carbon-based anti stiction layer at high temperatures. The results of our investigations suggest that the selection of the materials involved in a high temperature inertial sensor is especially critical and strongly affects the temperature sensitivity of the transducer. Temperature also affects the dynamic response of the sensor by decreasing the frequency of the dominant pole and the quality factor. These trends are coherent with expectations from squeeze film damping when the temperature dependence of viscosity and pressure of the damping fluid are included. Therefore, very low gas pressure levels inside the cavity might be a way to reduce the temperature effects on the dynamic sensor response.

5. Acknowledgements

This work has been funded by the Knut and Alice Wallenberg Foundation as a part of the Working on Venus project and by the European Research Council through the ERC Starting Grant M&M's (No. 277879). The authors acknowledge Miku Laakso for the valuable comments on the manuscript and ITmems for lending the characterization platform (MCP-G) used for the collection of the preliminary data (not presented here).

References

- [1] X. Jiang, K. Kim, S. Zhang, J. Johnson, G. Salazar, High-temperature piezoelectric sensing, *Sensors* 14 (1) (2013) 144–169. doi:doi:10.3390/s140100144.
- [2] R. Johnson, J. Evans, P. Jacobsen, J. Thompson, M. Christopher, The changing automotive environment: high-temperature electronics, *IEEE Transactions on Electronics Packaging Manufacturing* 27 (3) (2004) 164–176. doi:10.1109/TEPM.2004.843109.
- [3] J. Watson, G. Castro, High-Temperature Electronics Pose Design and Reliability Challenges, *Analog Devices* [cited September 25, 2015]. URL http://www.analog.com/library/analogDialogue/archives/46-04/high_temp_electronics.pdf
- [4] F. Rudolf, S. Gonseth, R. Brisson, P. Krebs, New generation of high performance/high reliability mems accelerometers for harsh environment, in: *Position, Location and Navigation Symposium-PLANS 2014*, 2014 IEEE/ION, IEEE, 2014, pp. 7–11. doi:doi:10.1109/PLANS.2014.6851350.
- [5] G. W. Hunter, J. D. Wrbanek, R. S. Okojie, P. G. Neudeck, G. C. Fralick, L. Chen, J. Xu, G. M. Beheim, Development and application of high-temperature sensors and electronics for propulsion applications, in: *Defense and Security Symposium*, International Society for Optics and Photonics, 2006, pp. 622209–622209. doi:doi:10.1117/12.668458.

- [6] E. J. Eklund, A. M. Shkel, Single-mask fabrication of high-g piezoresistive accelerometers with extended temperature range, *Journal of Micromechanics and Microengineering* 17 (4) (2007) 730. doi:doi:10.1088/0960-1317/17/4/009.
- [7] C.-H. Wu, C. Zorman, M. Mehregany, Fabrication and testing of bulk micro-machined silicon carbide piezoresistive pressure sensors for high temperature applications, *Sensors Journal, IEEE* 6 (2) (2006) 316–324. doi:10.1109/JSEN.2006.870145.
- [8] K. I. Lee, H. Takao, K. Sawada, M. Ishida, A three-axis accelerometer for high temperatures with low temperature dependence using a constant temperature control of SOI piezoresistors, in: *Micro Electro Mechanical Systems, 2003. MEMS-03 Kyoto. IEEE The Sixteenth Annual International Conference on, 2003*, pp. 478–481. doi:10.1109/MEMSYS.2003.1189790.
- [9] G. Salazar, K. Kim, S. Zhang, X. Jiang, Piezoelectric accelerometer for high temperature (1300 °C) sensing, in: *SPIE Smart Structures and Materials+ Nondestructive Evaluation and Health Monitoring, International Society for Optics and Photonics, 2012*, p. 83471k. doi:doi:10.1117/12.917104.
- [10] S. Tadigadapa, K. Mateti, Piezoelectric mems sensors: state-of-the-art and perspectives, *Measurement Science and Technology* 20 (9) (2009) 092001. doi:doi:10.1088/0957-0233/20/9/092001.
URL <http://stacks.iop.org/0957-0233/20/i=9/a=092001>
- [11] Analog Devices. ADXL206 datasheet [online, cited September 25, 2015].
URL <http://www.analog.com/media/en/technical-documentation/data-sheets/ADXL206.PDF>
- [12] D. Young, J. Du, C. Zorman, W. Ko, High-temperature single-crystal 3C-SiC capacitive pressure sensor, *Sensors Journal, IEEE* 4 (4) (2004) 464–470. doi:10.1109/JSEN.2004.830301.
- [13] Colibrys. Accelerometer for AHRS application - application note [online, cited September 25, 2015].
URL http://www.colibrys.com/wp-content/uploads/2015/03/30N.AHRS_.C.06.15.pdf
- [14] W. R. Ashurst, C. Carraro, R. Maboudian, Vapor phase anti-stiction coatings for MEMS, *Device and Materials Reliability, IEEE Transactions on* 3 (4) (2003) 173–178. doi:10.1109/TDMR.2003.821540.
- [15] A. Sherman, Growth and properties of LPCVD titanium nitride as a diffusion barrier for silicon device technology, *Journal of The Electrochemical Society* 137 (6) (1990) 1892–1897. arXiv:<http://jes.ecsdl.org/content/137/6/1892.full.pdf+html>, doi:10.1149/1.2086826.
URL <http://jes.ecsdl.org/content/137/6/1892.abstract>

- [16] M. Hopcroft, W. Nix, T. Kenny, What is the Young's modulus of silicon?, *Microelectromechanical Systems, Journal of* 19 (2) (2010) 229–238. doi: 10.1109/JMEMS.2009.2039697.
- [17] F. E. H. Tay, X. Jun, Y. C. Liang, V. J. Logeeswaran, Y. Yufeng, The effects of non-parallel plates in a differential capacitive microaccelerometer, *Journal of Micromechanics and Microengineering* 9 (4) (1999) 283. doi: doi:10.1088/1674-4926/30/3/034008.
- [18] S. D. Senturia, *Microsystem design*, Springer Science & Business Media, 2007.
- [19] J. Blech, On isothermal squeeze films, *Journal of Tribology* 105 (4) (1983) 615–620. doi:doi:10.1115/1.3254692.
- [20] T. Veijola, H. Kuisma, J. Lahdenperä, T. Ryhänen, Equivalent-circuit model of the squeezed gas film in a silicon accelerometer, *Sensors and Actuators A: Physical* 48 (3) (1995) 239–248. doi:doi:10.1016/0924-4247(95)00995-7.
- [21] Y. Okada, Y. Tokumaru, Precise determination of lattice parameter and thermal expansion coefficient of silicon between 300 and 1500 K, *Journal of Applied Physics* 56 (2) (1984) 314–320. doi:http://dx.doi.org/10.1063/1.333965. URL <http://scitation.aip.org/content/aip/journal/jap/56/2/10.1063/1.333965>
- [22] N. Ono, K. Kitamura, K. Nakajima, Y. Shimanuki, Measurement of Young's modulus of silicon single crystal at high temperature and its dependency on boron concentration using the flexural vibration method, *Japanese Journal of Applied Physics* 39 (2R) (2000) 368. doi:doi: 10.1143/JJAP.39.368.
- [23] Colibrys, Colibrys MS9000 series datasheet [cited September 25, 2015]. URL <http://www.colibrys.com/wp-content/uploads/2015/03/30S-MS9000.M.03.15-nod1.pdf>
- [24] J. C. Hecker, Scientific foundations of vacuum technique, *Journal of the American Chemical Society* 84 (15) (1962) 3032–3033. doi:doi:10.1021/ja00874a050.
- [25] W. Sutherland, LII. The viscosity of gases and molecular force, *The London, Edinburgh, and Dublin Philosophical Magazine and Journal of Science* 36 (223) (1893) 507–531. doi:doi:10.1080/14786449308620508.
- [26] D. R. Lide, *CRC Handbook of Chemistry and Physics*, CRC press, 2004.